# Adhesion of growing nanoparticles at a glance: Surface differential reflectivity spectroscopy and grazing incidence small angle x-ray scattering

R. Lazzari,[1] G. Renaud,[2] C. Revenant,[2] J. Jupille,[1] and Y. Borensztein[1]
[1]*Institut des NanoSciences de Paris, CNRS UMR 7588, Université Pierre et Marie Curie-Paris 6, Campus Boucicaut, 140 Rue de Lourmel, 75015 Paris, France*
[2]*CEA, INAC/SP2M/NRS, 17 Avenue des Martyrs, F-38054 Grenoble, France*
(Received 19 November 2008; revised manuscript received 17 February 2009; published 24 March 2009)

This paper compares the capability of surface differential reflectivity spectroscopy (SDRS) and grazing incidence small angle x-ray scattering (GISAXS) to characterize *in situ*, "at a glance," a collection of nanoclusters by statistically defining the geometry of an average particle (diameter, height, and interparticle distance). SDRS and GISAXS are run simultaneously on Ag/MgO(001) films during their growth. They are shown to lead to consistent values of the morphological parameters, with a particular good agreement about the aspect ratio (height/diameter) which, thanks to the basic physics underlying the two measurements, is determined in both cases. By modeling silver particles by truncated spheres, close estimates of the wetting angle and of the adhesion energy are derived ($0.75 \pm 0.08$ J m$^{-2}$ for SDRS and $0.85 \pm 0.20$ J m$^{-2}$ for GISAXS). This demonstrates that the very flexible laboratory SDRS can be used to study the growth of a film in a similar way as the well-documented small angle x-ray scattering provided it is analyzed in an appropriate framework.

DOI: 10.1103/PhysRevB.79.125428 PACS number(s): 68.47.Jn, 68.55.A−, 78.67.Bf, 61.05.cf

## I. INTRODUCTION

Nanoparticles are often involved in macroscopic objects which they functionalize. The *in situ* and *in real time* characterization of vast collection of particles to control either the manufacturing or the behavior of such objects is one of the most crucial issues of nanoscience.[1,2] For local analysis at the scale of the nanometer, widely used approaches are imaging techniques such as electron microscopy and near-field microscopy. However, these methods have some drawbacks such as (i) the difficulty for *in situ* implementation during the growth process and (ii) the limitation of the analysis to a microscopic part of the sample only, which in some cases might be misleading. Indeed, microscopic approaches do not have the capability to characterize "at a glance" a collection of nanoclusters by statistically defining an average representative particle.

Light, including x rays, is a probe of relevance to control nanoparticles spread over a macroscopic sample within any transparent environment. In the particular case of thin films made of particles growing on a surface, the ability of surface differential reflectivity spectroscopy (SDRS)[2–8] and grazing incidence small angle x-ray scattering (GISAXS)[1,9–11] to characterize an assembly of nanoclusters was proved by performing data analysis in an appropriate manner.[12,13] Those very flexible and nondestructive methods can be run in any conditions of pressure or temperature for particles either supported by a substrate or embedded in a transparent matrix and, because they are free of charging effects, on insulators. SDRS (Refs. 14 and 15) compares to ellipsometry. Upon deposition, the morphology of nanoparticles is probed via the modification of the Fresnel reflectivity (dielectric properties) of the surface. In the case of the metal/oxide cluster growth, the signal arises from the so-called Mie absorption or plasmon resonance[16] which is due to a combination of the field-induced polarization of the electronic gas of the metal clusters and of the damping of the vibrating dipole. The key parameter in the modeling of the resonance is the island polarizability.[16] It depends on the cluster shape through the depolarization factor and on the image dipole inside the substrate.[16,3,5–7] Accounting for the shift in resonance energy that stems from the coupling between individual dipoles gives access to the cluster density.[7,8] Based on the determination of characteristic lengths in the reciprocal space, GISAXS analyzes the morphology and distribution of nanoparticles.[17–25] GISAXS has emerged as a powerful tool to study surface roughness,[26,27] lateral correlations, sizes and shapes of quantum dots,[28–31] discontinuous multilayers,[22] self-organized dot superlattices[32,33] or wires.[34] Ultrahigh vacuum (UHV) GISAXS measurements have been recently performed *in situ* and during the growth of nanoparticles on surfaces, in conditions yielding very high sensitivity and background-free data.[1,35,9–11]

Since SDRS and GISAXS both aim at defining an average supported cluster, measurements can be directly compared. Relying on the widespread diffraction physics, GISAXS is *a priori* considered as quantitative. Very different is the case of SDRS, which is based on assumptions which reliability has to be tested. In the present work, SDRS and GISAXS data are collected *in situ* and at the same time on growing Ag/MgO(001) films. This system is an archetype of three-dimensional (Volmer-Weber) growth[36,37] and silver is optimal for both measurements since it provides sharp plasmon resonances for SDRS analysis and a heavy Z element for x-ray scattering. The capability of SDRS and GISAXS to accurately determine particle size, shape and density and, further, the adhesion energy, is then discussed.

## II. EXPERIMENTS

### A. Instruments

The measurements were performed at the European Synchrotron Radiation Facility (ESRF) on the ID32 undulator

 

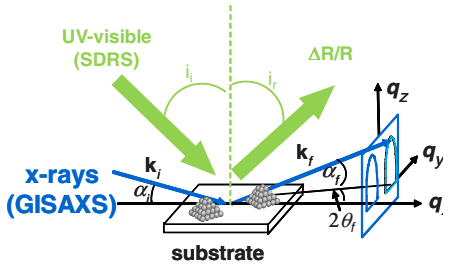


FIG. 1. (Color online) Principle of the coupled SDRS and GISAXS measurements. In SDRS, the relative variation in the sample reflectivity in the UV-visible range is recorded. The incident and reflection angles are related by the Snell-Descartes law: $i_i=i_r$. In GISAXS, the incident x-ray beam of wave vector $\boldsymbol{k}_i$ impinges on the surface at a grazing angle $\alpha_i$. The scattered intensity (wave vector $\boldsymbol{k}_f$) is recorded on a plane as function of the exit angle $\alpha_f$ (with respect to the surface plane) and of the in-plane angle $2\theta_f$. The wave vector transfer is noted $\boldsymbol{q}=(q_x,q_y,q_z)$.

beamline.[38] A dedicated experimental setup was developed to simultaneously perform GISAXS and SDRS *in situ* measurements in UHV during the growth of a supported film.[35]

The principle of the double measurement is schematized in Fig. 1. SDRS is performed by collimating the light emitted by a deuterium lamp in the UV-visible range (1.5 to 6 eV) on the sample with an incident angle of $i_i=i_r=55°$ (measured from the sample normal as usual in optics). The specular beam is collected in *p* polarization, i.e., with the electric field in the plane of incidence. It is then dispersed by a grating spectrograph (300 grooves/mm) on a Peltier-cooled photodiode array. The incident and scattered lights travel through the vacuum chamber via transparent silica windows. The parameter which is examined is the relative variation of the sample reflectivity, with reference to the substrate reflectivity $R_0$ before deposition:

$$\frac{\Delta R}{R}=\frac{R-R_0}{R_0}. \tag{1}$$

To perform GISAXS, the x-ray beam is shone on the surface at a grazing incidence (measured from the sample surface as usual in x-ray optics). The scattered intensity is measured at small angle around the direct and specular beams, which are hidden by a beam stop. Denoting $\alpha_i$ (resp. $\alpha_f$) the incident (resp. exit) angle with respect to the sample surface, $2\theta_f$ the in-plane scattering angle parallel to the surface (Fig. 1), and λ the x-ray wavelength, the wave vector transfer $\mathbf{q}=\mathbf{k}_f-\mathbf{k}_i$ is given by

$$\mathbf{q}=\begin{pmatrix} q_x \\ q_y \\ q_z \end{pmatrix}=\frac{2\pi}{\lambda}\begin{pmatrix} \cos(\alpha_f)\cos(2\theta_f)-\cos(\alpha_i) \\ \cos(\alpha_f)\sin(2\theta_f) \\ \sin(\alpha_f)+\sin(\alpha_i) \end{pmatrix}, \tag{2}$$

$q_y$ (resp. $q_z$) is the momentum transfer component parallel (resp. perpendicular) to the surface and perpendicular to the incident beam. At small angles, $q_x\sim 0$ and $q_y \sim(2\pi/\lambda)\sin(2\theta_f)$. The origin of the out-of-plane exit angle $\alpha_f$, which lies between the direct beam and the specular beam, is determined by recording an image without beam stop. To enhance the signal from the film, the incident angle was taken close to the critical angle of the substrate. A Peltier-cooled high grade 16-bit two-dimensional (2D) charge coupled device detector (Photonic Science) of 1152 $\times$1242 pixels of (67 $\mu$m)$^2$ size was located at a distance of $\sim$1 m from the sample. At the sample position, the beam size was $0.5\times 0.2$ mm$^2$ [H$\times$V, full width at half maximum (FWHM)] with divergence of $2\times 10^{-5}$ rad (H,FWHM) and $4\times 10^{-6}$ rad (V,FWHM) and a flux $>10^{12}$ photons/s. The aperture of the detector ($77\times 83$ mm$^2-3.26\times 4.2°$) and the beam stop size (1 mm) in front of the detector correspond to minimal and maximal real space distances along $q_y$ of 1.5 nm and 225 nm, respectively.

### B. Samples

The $15\times 15\times 0.5$ mm$^3$ MgO(001) substrates supplied by Earth Chemical Co. Ltd. (Tokyo, Japan) were prepared by annealing in air followed by ion bombardment at high temperature (1770 K) in vacuum, fast cooling down and moderate annealing under oxygen partial pressure ($p\sim 10^{-5}$ mbar) to obtain wide (001) terraces free of contaminants.[39] Experiments were performed in a vacuum chamber (base pressure $\sim 2\times 10^{-10}$ mbar) coupled to the ID32 undulator beamline.[35] The temperature of the sample was measured by means of a pyrometer. Silver was deposited using a Knudsen cell operated at 1120 K under a working pressure of $4\times 10^{-10}$ mbar. The flux was $\sim$0.1 nm/min, as estimated by a quartz microbalance.

## III. GROWTH AT A GLANCE

The growth of Ag/MgO(001) at 300 and 640 K was simultaneously characterized *in situ* by SDRS and GISAXS.

### A. SDRS

The optical spectra recorded during the Ag/MgO(001) growth at 300 and 640 K are reported in Fig. 2 for different deposited thicknesses. They exhibit a broad positive resonance at photon energy around 2.5 eV, and a narrow negative resonance at 3.8 eV (Fig. 2) which are associated to the dipolar-type plasmon resonances excited in the particles in directions parallel (peak at 2.5 eV) and perpendicular (peak at 3.8 eV) to the substrate, respectively.[40,4–6,41] These positive/negative features are related to the geometry of the experiment, with *p*-polarized light exciting both resonances. Moreover, a fingerprint of interparticle coupling of quadrupolar character shows up ca. 3.5 eV.[7,8] The negative resonance around 3.8 eV located close to the bulk plasmon energy of silver only slightly depends on the shape of the particles. Within the quasistatic approximation, i.e., for particles much smaller than the wavelength of light, this resonance can shift from 3.5 eV for spherical particles to 3.8 eV for flat ones. Quite differently, the positive low-energy resonance which corresponds to the parallel component of the field-induced dipole is extremely sensitive to the shape of the particle. This resonance shifts continuously from 3.5 eV for spheres to energy lower than 2 eV (limit of the present analysis) for very flat particles.[16] The average position of this resonance located around 2.5 eV indicates a three-dimensional

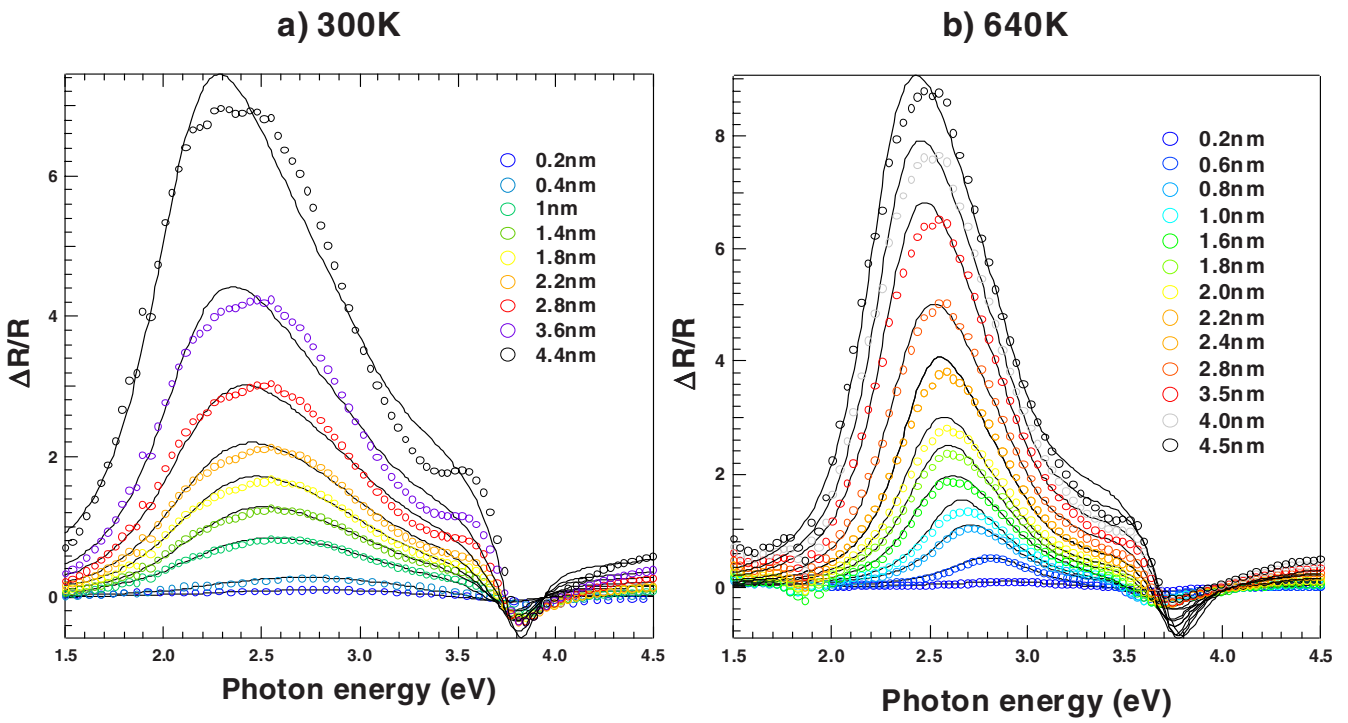


FIG. 2. (Color online) SDRS optical spectra recorded *in situ* during the growth of the Ag/MgO(001) film at (a) 300 and (b) 640 K. Deposited thicknesses are given—Open circles: experiment; line: simulation (see text).

growth mode.[6,4] Because $\Delta R/R$ is governed by the imaginary part of the cluster polarizability which depends on the cluster shape through the depolarization factor and on the image dipole inside the substrate,[16,42] the fit of the signal to an appropriate model leads directly to an estimate of the average aspect ratio $H/D$ of the particles.

In order to fit SDRS spectra, the Fresnel reflectivity was modeled in the framework of the surface susceptibilities developed by Bedeaux and Vlieger (see Ref. 42 and all references therein). These are related to the particle polarizabilities along the parallel and perpendicular directions. In the present case, they were calculated through multipolar expansion techniques[43,5,8,42] in the quasistatic approximation (i.e., under the assumption of particle smaller than the wavelength of the light). The silver islands were represented by truncated spheres which is a well-adapted modeling when the aspect ratio $H/D$ is higher than 0.5.[5] Particles with smaller aspect ratio are better represented by truncated ellipsoids.[6] The polarizabilities were renormalized by the particle-particle interaction up to dipolar order, a cutoff that was shown to be accurate up to a high surface coverage of 60%.[42] The dielectric constant of the metal is corrected from finite-size effects such as the reduced plasmon lifetime[16] and the quantum blueshift of the resonance due to a smaller interaction between *s* and *d* electrons of silver at surfaces.[3,44] It is assumed that the film is well accounted for by monodisperse particles, although in actual measurements, an inhomogeneous broadening of the plasmon resonances comes from a distribution of sizes and aspect ratios. These are accounted for in an effective way by folding the imaginary part of the polarizability with a Gaussian peak. Its FWHM is nearly constant all along the growth (0.8 eV at 300 K; 0.35 eV at 640 K). The experimental spectra (Fig. 2) are fitted by using the GRANFILM software.[12,45] A $\chi^2$ minimization is performed at a multipolar order chosen to numerically converge,[5] typically $M=16$. The resulting morphological parameters (particle diameter $D$, particle height $H$, and interparticle distance $L$) are given in Fig. 3 and the aspect ratio $H/D$ in Fig. 4. $H/D$ is directly determined by SDRS.

### B. GISAXS

GISAXS measurements were performed with x rays of 0.1127 nm wavelength at an incidence equal to the critical angle for total external reflection ($\alpha_c=0.20°$) and with the incident x-ray beam along the [010] and [$1\bar{1}0$] directions of the MgO(001) substrate, i.e., with $q_y$ along the [100] and [110] crystallographic directions, respectively. GISAXS patterns (Fig. 5) show two intensity maxima in the parallel direction, on each side of the specular reflection. Because of refraction and reflection effects,[46,47] the off-specular diffuse scattering intensity, also called Yoneda peak, is maximum when $\alpha_f$ is equal to the critical angle for total external reflection (Fig. 1).

When growth proceeds, the shrinking of the pattern toward the origin reveals an increase in all dimensions in real space, since the width, height, and separation distance of the scattered lobes are inversely proportional to $D$, $H$, and $L$, respectively. For large enough thickness, the second- and third-order maxima in the perpendicular direction (for Ag coverage higher than 2.2 nm) are indicative of a narrow distribution of the island height $H$. Upon further increase in coverage, these maxima vanish until the GISAXS pattern looks like an apex [Fig. 5(h)], showing that the islands become flatter. This corresponds to the coalescence regime, during which neighboring particles merge to give rise to

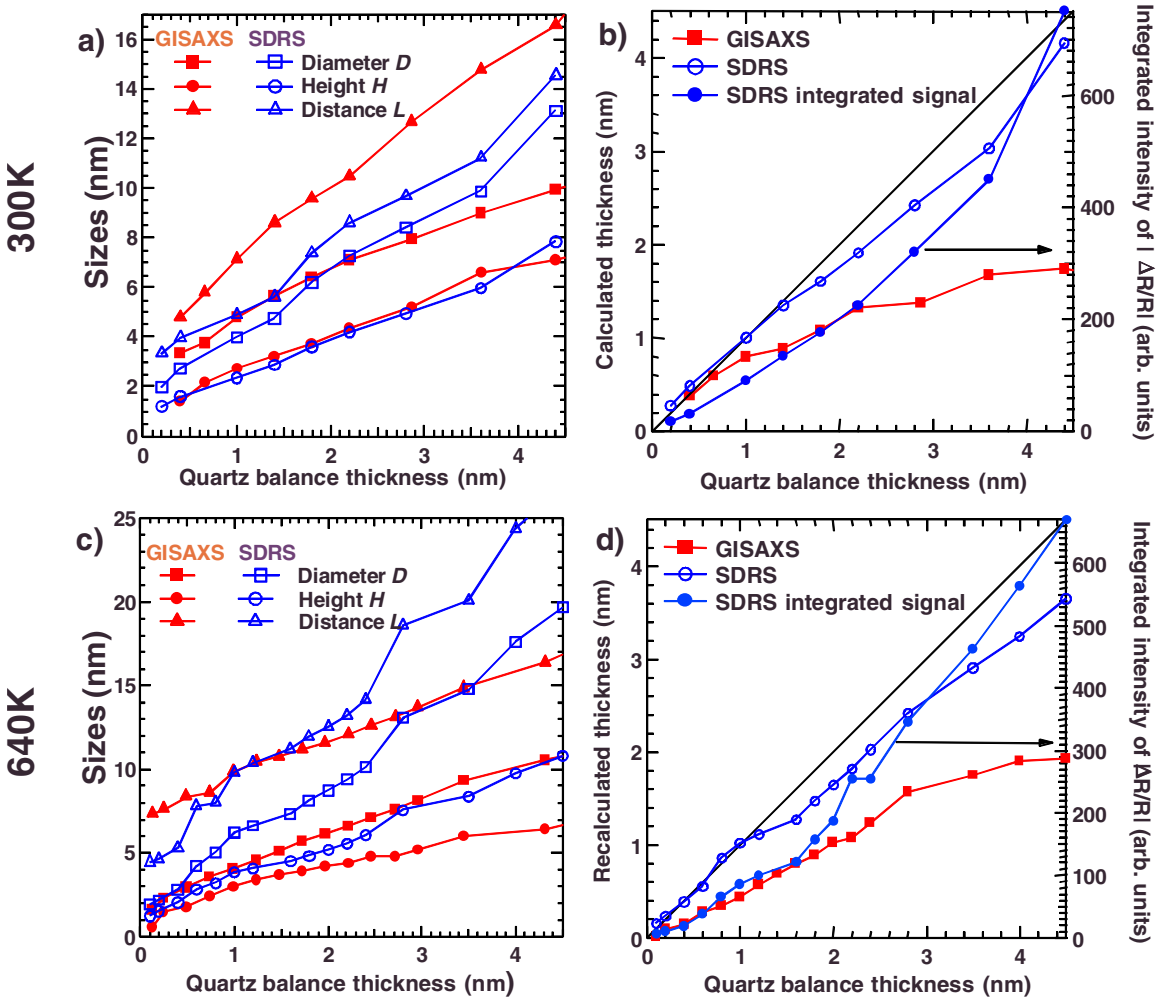


FIG. 3. (Color online) Evolution of the morphological parameters $H$, $D$, and $L$ (a) and (b) at 300 (c) and (d) at 640 K. Filled symbol: GISAXS; open symbol: SDRS—Estimates of the thickness obtained from $H$, $D$, $L$ are shown in (b) and (d) as a function of the quartz measurements. The SDRS integrated signal (filled circles) over the whole spectral range is shown on the right scale of (b) and (d). To first approximation, it depends linearly on the film thickness (Ref. 42).

large flat islands exposing a top {001} surface and side {111} facets.[48]

The $D$, $H$, and $L$ values were derived from the GISAXS data by modeling silver particles by spheres (to analyze the in-plane data) or cylinders (for out-of-plane data).[20,23,24] To speed up the fitting process, size distribution, multiple scattering on the substrate,[9,13,49] and change in the gradient of dielectric index[11,50] were neglected. Two intensity cuts along the $(q_y, q_z)$ plane were fitted, one parallel to the surface at the $q_z$ position of maximum intensity, and the other perpendicular to it at the $q_y$ position of the interference maximum. In the direction parallel to the surface, the experimental GISAXS intensity $I(q_y)$ was fitted with the following function:

$$I(q_y) = A_{\mathrm{par}} F^2_{\mathrm{sph}}(q_y) S(q_y), \tag{3}$$

where $A_{\mathrm{par}}$ is a scale factor, $F_{\mathrm{sph}}(q_y)$ is the form factor (i.e., the amplitude of the Fourier transform) of a hemisphere,[51] and $S(q_y)$ is the interference function of the nanocluster assembly. This interference function was modeled by an *ad hoc* function (see the Appendix), which was found to satisfactorily fit the interference functions calculated from typical transmission electron microscopy (TEM) plane views of several Ag/MgO(001) and Pd/MgO(001) deposits.[9,52] In the perpendicular direction, the experimental GISAXS intensity $I(q_z)$ is fitted for cylindrical particles by

$$I(q_z) = A_{\mathrm{per}} F^2_{\mathrm{cyl}}(q_z) T(q_z) e^{-Bq_z^2}, \tag{4}$$

where $A_{\mathrm{per}}$ is a scale factor, $F_{\mathrm{cyl}}(q_z)$ is the form factor of a cylinder,[51] and $B$ is an attenuation parameter accounting for the distribution of heights. Because the islands are small, the multiple scattering effects due to reflections on the substrate, which are usually treated by the distorted wave Born approximation for particles on a substrate,[49] are satisfactorily taken into account by multiplying the particle form factor by the ratio $T(q_z)$ of the transmitted and incident x-ray intensities, which are the results of the DWBA for particles buried below the surface.[47] The analytical expressions for these functions are given in the Appendix. Figure 6 shows a typical example of such data analysis. The intensity maxima parallel

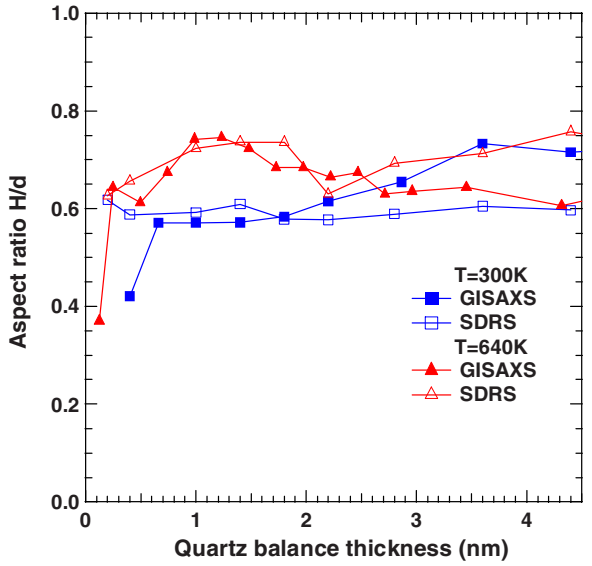


FIG. 4. (Color online) Values of the aspect ratio of Ag/MgO(001) clusters grown at 300 and 640 K. They are directly determined in the case of SDRS data. In the case of GISAXS, they are derived from the particle heights and diameters shown in Fig. 3.

to the surface and the positions of the maxima perpendicular to the surface are well reproduced. However, the absence of size distributions yields oscillations in intensity that are absent from the experimental data. The obtained parameters $D$, $H$, $L$, and $H/D$ are gathered in Figs. 3 and 4.

## IV. COMPARISON BETWEEN SDRS AND GISAXS RESULTS

The interest in the determination of the shape of supported particles is the characterization of their adhesion (wetting) properties. The adhesion energy $E_{adh}$ can be determined either by means of a Wulff construction[1,9] or, as discussed herein, via the modeling of the particles by truncated spheres

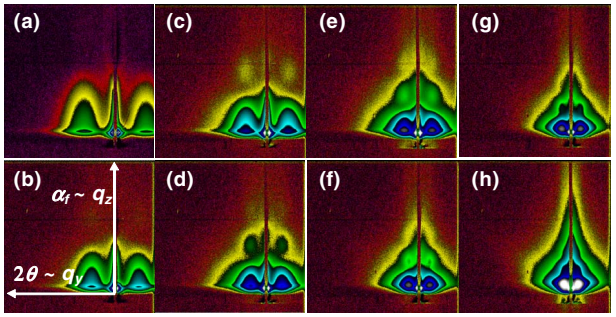


FIG. 5. (Color online) Evolution of the 2D GISAXS patterns recorded *in situ* during the Ag/MgO(001) growth at 300 K (simultaneously with SDRS), with the incident beam parallel to the MgO[010] direction, as a function of the deposited thickness: (a) 1 nm, (b) 1.8 nm, (c) 2.2 nm, (d) 3.6 nm, (e) 4.4 nm, (f) 6.2 nm, (g) 7 nm, and (h) 10 nm. The intensity is represented on a logarithmic scale. Black contours between colors correspond to order of magnitude in intensity. The $q_y$ (respectively, $q_z$) axis ranges from 0 to 2.5 $nm^{-1}$ (respectively, 2.6 $nm^{-1}$).

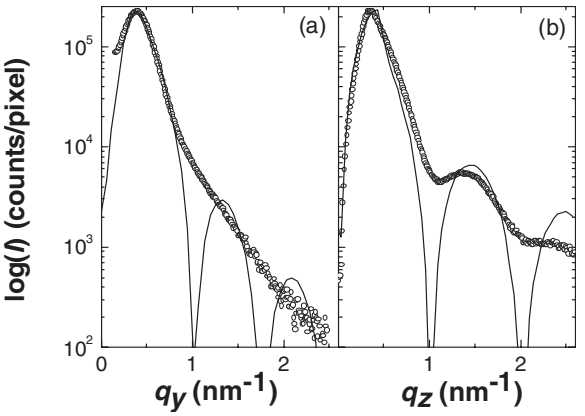


FIG. 6. GISAXS cut (a) parallel and (b) perpendicular to the surface for the 3.6-nm-thick Ag deposit on MgO(001) at 300 K. Dots: cuts of the experimental GISAXS pattern; thin line: best fits of the experimental cuts. The results of the best fit are as follows: $L=14.2$ nm, $D=8.8$ nm, and $H=6.3$ nm. The intensity is represented on a logarithmic scale.

to derive an average wetting angle to apply the Young-Dupré formula $E_{adh}=\sigma_{Ag}\ (1+\cos\ \phi)$.[2,53,54] The crucial point is to accurately determine the aspect ratio $H/D$, which is not straightforward by using microscopy techniques. Known difficulties are the measurement of the particle diameter in near-field microscopy (it can be multiplied by a factor 2.5 to 1.5 for 2–6 nm particles[55] due to the so-called tip artifact) and the estimate of the particle height from the observation of a collection of particles by TEM.

In this context, the common advantage of SDRS and GISAXS is that they both allow a direct determination of the aspect ratio $H/D$, in the direct and reciprocal space, respectively (see above). In Fig. 4, the striking observation is the close agreement of the SDRS and GISAXS values of aspect ratios, except at very low coverage where the discrepancy might arise from the limitation by the aperture of the GISAXS detector to particles of size $\geq 1$ nm (see below) as well as from the difficulty to model the blueshift of the optical response of small silver particles.[44] The SDRS vs GISAXS agreement at all temperatures and coverages demonstrates the consistency of the two methods. Moreover, it conclusively proves the reliability of SDRS when analyzed on the above-mentioned physical basis and its relevance for a quantitative description of the geometry of supported nanoparticles.

By modeling particles by truncated spheres, wetting angles are derived from the average values of the aspect ratio determined at 640 K (Table I), a temperature at which clusters are likely close to equilibrium. Then, by taking $\sigma_{001}=1.20$ J $m^{-2}$ for the surface energy of Ag(001) [theoretical value[56] close to the experimental estimate of 1.18 J $m^{-2}$ for polycrystalline silver at 640 K (Ref. 57)], very similar values of $0.75\pm0.08$ J $m^{-2}$ and $0.85\pm0.20$ J $m^{-2}$ are found for the adhesion energy of Ag/MgO(001) by SDRS and GISAXS, respectively (Table I). This is to be compared to 0.45 J $m^{-2}$ determined via a contact angle measurement by TEM (Ref. 48) and $0.3\pm0.3$ J $m^{-2}$ derived from the measurement of the heat of adsorption.[58] The scattering of results can be ex-

TABLE I. Average aspect ratios of Ag/MgO(001) particles as determined from SDRS and GISAXS data (Fig. 4). Error bars are given by standard deviations. Wetting angles and adhesion energies are derived from these values (see text).

| | Aspect ratios $H/D$ | | Wetting angle in degrees (energy of adhesion in J m$^{-2}$) | | Energy of adhesion (J m$^{-2}$) from shape analysis in GISAXS[a] |
|---|---|---|---|---|---|
| Ag/MgO(001) | SDRS | GISAXS | SDRS | GISAXS | |
| Growth at 300 K | $0.59 \pm 0.02$ | $0.60 \pm 0.10$ | | | |
| Growth at 640 K | $0.69 \pm 0.02$ | $0.65 \pm 0.08$ | $112 \pm 4$ $(0.75 \pm 0.08)$ | $107 \pm 10$ $(0.85 \pm 0.20)$ | $0.80 \pm 0.10$ |

[a]Reference 52.

plained by the crucial role played by charged defects and impurities at metal-ceramic interface.[59,60] Indeed, the adhesion properties strongly depend on the sample preparation. The theoretical values, which range from 0.26 J m$^{-2}$ to 1.6 J m$^{-2}$,[61–64,59,65] are even more scattered than experimental data.

Some limits of the measurements are revealed by the detailed examination of the parameters that are derived from GISAXS and SDRS, in particular the average thickness. As expected for noninteracting particles of given shape ($H/D$ ~constant, Fig. 4),[7] the differential reflectivity $\Delta R/R$ integrated over the plasmon resonance band (a quantity governed by the imaginary part of the cluster polarizability) is, to a first approximation, proportional to the mean thickness [Figs. 3(b) and 3(d)]. In passing, the nice agreement of the SDRS estimate with the quartz measurement shows that, at 300 and 640 K, the sticking probability of silver on bare MgO(001) is close to unity, consistently with the results of Larsen *et al.*[58] The agreement is less good in the case of GISAXS. Due to the way the average thickness is calculated from GISAXS data ($\sim HD^2L^{-2}$), small shifts in $D$ and $L$ values strongly affect its estimate. Moreover, the scattered x-ray beam is collected outside the beam stop and within the detector aperture which imposes upper and lower values of the lateral size of the clusters. For example, in the geometry used at 300 K, GISAXS probes particles which diameter ranges between ~1 and 18 nm. The latter value likely explains why the silver coverage deduced from GISAXS levels off above ~3 nm [Figs. 3(b) and 3(d)].

The particle height, particle diameter, and interparticle distance are very similar at any silver coverage for the film grown at 300 K [Fig. 3(a)], but they show discrepancies up to 40% at 640 K [Fig. 3(b)]. Discrepancies on $H$ and $L$ can be partly explained by their indirect derivation in SDRS; only $D/H$ and the film thickness are directly determined as $\Delta R/R$ is proportional to the film thickness and the polarizabilities depend mainly on the particle aspect ratio.[4–7]

## V. CONCLUSION

The evolution of the Ag/MgO(001) particle morphology has been simultaneously investigated *in situ*, during the growth, by GISAXS and SDRS experiments at different temperatures.

(1) Coverage—The SDRS integrated intensity is approximately proportional to the average thickness and can be used as a quantitative probe of the coverage. GISAXS intensity is not such an easy cut since it arises from clusters which size is within the range allowed by the detector aperture. This excludes very small islands which scatter outside that aperture and very large islands which scatter within the beam stop.

(2) Aspect ratio and adhesion energy—Within the limits which are discussed herein, which mostly arise from the discrepancies about the coverage, SDRS and GISAXS lead to similar descriptions of the average particle geometry. A particularly good agreement is found about aspect ratios, so that consistent estimates of the Ag/MgO(001) adhesion energy are found by representing silver clusters by truncated spheres [$0.75 \pm 0.08$ J m$^{-2}$ (SDRS) and $0.85 \pm 0.20$ J m$^{-2}$ (GISAXS)].

SDRS and GISAXS can be run *in situ* during the growth of films to observe "at a glance, close to *real time*, a vast collection of particles scattered on a macroscopic sample and to represent it by an average particle. The agreement found herein between the two methods demonstrates the reliability of the very flexible SDRS measurements by comparison with the well known GISAXS, provided the optical response is interpreted by means of the appropriate models. This is especially interesting at the initial stage of film growth since SDRS is by far much more sensitive than GISAXS at submonolayer coverage.

## ACKNOWLEDGMENTS

We would like to thank the staff of the ESRF ID32 beamline for their help during the GISAXS setup and measurements. SP2M is a laboratory associated with the Université Joseph Fourier, Grenoble, France.

## APPENDIX

In the direction parallel to the surface, the form factor of a (hemi-)sphere (scaled by its volume) is simply given by

$$F_{\mathrm{sph}}(q_y) = 3\frac{\sin\left(q_y\frac{D}{2}\right) - q_y\frac{D}{2}\cos\left(q_y\frac{D}{2}\right)}{\left(q_y\frac{D}{2}\right)^3}. \quad \text{(A1)}$$

The *ad hoc* interference function[9] was defined by

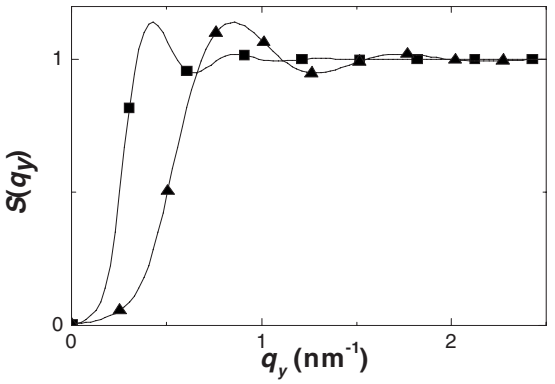


FIG. 7. Interference function $S(q_y)$. Filled squares: $L=14.2$ nm. This case corresponds to the 3.6-nm-thick Ag deposit on MgO(001) at 300 K. The corresponding GISAXS cut parallel to the surface is displayed in Fig. 6. Filled triangles: $L=7.1$ nm.

$$S(q_y) = E(q_y) + e^{-q_y L/\pi}\cos(q_y L)E(q_y) \tag{A2}$$

with

$$E(q_y) = 1 - \frac{1}{1 + e^{2L(q_y - \pi/L)}}. \tag{A3}$$

Figure 7 shows $S(q_y)$ for two typical values of the average interisland distance $L$, which is the only free parameter.

In the perpendicular direction, the form factor of a cylinder is

$$F_{\mathrm{cyl}}(q_z) = \frac{\sin(q_z H/2)}{q_z H/2} \tag{A4}$$

and the ratio of the transmitted and incident x-ray intensities is

$$T(q_z) = \frac{4\lambda^2 q_z^2}{(\lambda q_z + a)^2 + b^2} \tag{A5}$$

with

$$a = 0.5\sqrt{\sqrt{(\lambda^2 q_z^2 - 2\delta)^2 + 4\beta^2} + \lambda^2 q_z^2 - 2\delta},$$

$$a = 0.5\sqrt{\sqrt{(\lambda^2 q_z^2 - 2\delta)^2 + 4\beta^2} - \lambda^2 q_z^2 + 2\delta}. \tag{A6}$$


[1] G. Renaud, R. Lazzari, C. Revenant, A. Barbier, M. Noblet, O. Ulrich, F. Leroy, J. Jupille, Y. Borensztein, C. R. Henry, J.-P. Deville, F. Scheurer, J. Mane-Mane, and O. Fruchart, Science **300**, 1416 (2003).
[2] R. Lazzari and J. Jupille, Phys. Rev. B **71**, 045409 (2005).
[3] Y. Borensztein, P. De Andrès, R. Monreal, T. Lopez-Rios, and F. Flores, Phys. Rev. B **33**, 2828 (1986).
[4] R. Lazzari, J. Jupille, and Y. Borensztein, Appl. Surf. Sci. **142**, 451 (1999).
[5] I. Simonsen, R. Lazzari, J. Jupille, and S. Roux, Phys. Rev. B **61**, 7722 (2000).
[6] R. Lazzari, I. Simonsen, D. Bedeaux, J. Vlieger, and J. Jupille, Eur. Phys. J. B **24**, 267 (2001).
[7] R. Lazzari, S. Roux, I. Simonsen, J. Jupille, D. Bedeaux, and J. Vlieger, Phys. Rev. B **65**, 235424 (2002).
[8] R. Lazzari, I. Simonsen, and J. Jupille, Europhys. Lett. **61**, 541 (2003).
[9] C. Revenant, F. Leroy, R. Lazzari, G. Renaud, and C. R. Henry, Phys. Rev. B **69**, 035411 (2004).
[10] J. Olander, R. Lazzari, J. Jupille, B. Mangili, J. Goniakowski, and G. Renaud, Phys. Rev. B **76**, 075409 (2007).
[11] R. Lazzari, G. Renaud, J. Jupille, and F. Leroy, Phys. Rev. B **76**, 125412 (2007).
[12] R. Lazzari and I. Simonsen, Thin Solid Films **419**, 124 (2002).
[13] R. Lazzari, J. Appl. Crystallogr. **35**, 406 (2002).
[14] Y. Borensztein, Surf. Rev. Lett. **7**, 399 (2000).
[15] P. Chiaradia and R. Del Sole, Surf. Rev. Lett. **6**, 517 (1999).
[16] U. Kreibig and M. Vollmer, *Optical Properties of Metal Clusters* (Springer-Verlag, Berlin, 1995).
[17] J. R. Levine, J. B. Cohen, Y. W. Chung, and P. Georgopoulos, J. Appl. Crystallogr. **22**, 528 (1989).
[18] J. R. Levine, J. B. Cohen, and Y. W. Chung, Surf. Sci. **248**, 215 (1991).
[19] A. Naudon, D. Babonneau, D. Thiaudière, and S. Lequien, Physica B **283**, 69 (2000).
[20] A. Naudon and D. Thiaudière, J. Appl. Crystallogr. **30**, 822 (1997).
[21] A. Naudon, T. Slimani, and P. Goudeau, J. Appl. Crystallogr. **24**, 501 (1991).
[22] D. Thiaudière, O. Proux, J.-S. Micha, C. Revenant, J.-R. Regnard, and S. Lequien, Physica B **283**, 114 (2000).
[23] D. Babonneau, F. Petroff, J.-L. Maurice, F. Fettar, A. Vaurès, and A. Naudon, Appl. Phys. Lett. **76**, 2892 (2000).
[24] D. Babonneau, I. R. Videnovic, M. G. Garnier, and P. Oelhafen, Phys. Rev. B **63**, 195401 (2001).
[25] B. Lairson, A. Payne, S. Brennan, N. Rensing, B. Daniels, and B. Clemens, J. Appl. Phys. **78**, 4449 (1995).
[26] V. Holý and T. Baumbach, Phys. Rev. B **49**, 10668 (1994).
[27] V. Holý, J. Kuběna, I. Ohlídal, K. Lischka, and W. Plotz, Phys. Rev. B **47**, 15896 (1993).
[28] T. H. Metzger, I. Kegel, R. Paniago, and J. Peisl, J. Phys. D **32**, A202 (1999).
[29] T. H. Metzger, I. Kegel, R. Paniago, A. Lorke, J. Peisl, J. Schulze, I. Eisele, P. Schittenhelm, and G. Abstreiter, Thin Solid Films **336**, 1 (1998).
[30] J. Stangl, V. Holý, P. Mikulik, G. Bauer, I. Kegel, T. H. Metzger, O. G. Schmidt, C. Lange, and K. Eberl, Appl. Phys. Lett. **74**, 3785 (1999).
[31] K. Zhang, C. Heyn, W. Hansen, T. Schmidt, and J. Falta, Appl. Surf. Sci. **175-176**, 606 (2001).
[32] J. Stangl, V. Holý, T. Roch, A. Daniel, G. Bauer, J. Zhu, K. Brunner, and G. Abstreiter, Phys. Rev. B **62**, 7229 (2000).
[33] V. Holý, J. Stangl, G. Springholz, M. Pinczolits, and G. Bauer, J. Phys. D **34**, A1 (2001).
[34] V. Holý, T. Roch, J. Stangl, A. Daniel, G. Bauer, T. H. Metzger, Y. H. Zhu, K. Brunner, and G. Abstreiter, Phys. Rev. B **63**, 205318 (2001).
[35] G. Renaud, M. Ducruet, O. Ulrich, and R. Lazzari, Nucl. In-

strum. Methods Phys. Res. B **222**, 667 (2004).
[36] O. Robach, G. Renaud, and A. Barbier, Phys. Rev. B **60**, 5858 (1999).
[37] G. Renaud, Surf. Sci. Rep. **32**, 5 (1998).
[38] ESRF, http://www.esrf.eu
[39] O. Robach, G. Renaud, and A. Barbier, Surf. Sci. **401**, 227 (1998).
[40] D. Martin, F. Creuzet, J. Jupille, Y. Borensztein, and P. Gadenne, Surf. Sci. **377-379**, 958 (1997).
[41] R. Lazzari and J. Jupille, Surf. Sci. **482-485**, 823 (2001).
[42] D. Bedeaux and J. Vlieger, *Optical Properties of Surfaces* (Imperial College Press, London, 2001).
[43] M. M. Wind, J. Vlieger, and D. Bedeaux, Physica A **141**, 33 (1987).
[44] A. Liebsch, Phys. Rev. B **48**, 11317 (1993).
[45] R. Lazzari and I. Simonsen, http://www.insp.upmc.fr/axe2/Oxydes/GranFilm/GranularFilm.html
[46] S. K. Sinha, E. B. Sirota, S. Garoff, and H. B. Stanley, Phys. Rev. B **38**, 2297 (1988).
[47] M. Rauscher, T. Salditt, and H. Spohn, Phys. Rev. B **52**, 16855 (1995).
[48] A. Trampert, F. Ernst, C. P. Flynn, H. F. Fischmeister, and M. Rühle, Acta Metall. Mater. **40**, S227 (1992).
[49] M. Rauscher, R. Paniago, T. H. Metzger, Z. Kovats, J. Domke, J. Peisl, H. D. Pfannes, J. Schulze, and I. Eisele, J. Appl. Phys. **86**, 6763 (1999).
[50] R. Lazzari, F. Leroy, and G. Renaud, Phys. Rev. B **76**, 125411 (2007).
[51] A. Guinier, *X-Ray Diffraction in Crystals, Imperfect Crystals, and Amorphous Bodies* (Dover, New York, 1963).
[52] C. Revenant, G. Renaud, R. Lazzari, and J. Jupille (unpublished).
[53] C. T. Campbell, Surf. Sci. Rep. **27**, 1 (1997).
[54] C. Henry, Surf. Sci. Rep. **31**, 231 (1998).
[55] Sh. K. Shaikhutdinov, R. Meyer, M. Naschitzki, M. Bäumer, and H.-J. Freund, Catal. Lett. **86**, 211 (2003).
[56] L. Vitos, A. V. Ruban, H. L. Skriver, and J. Kollar, Surf. Sci. **411**, 186 (1998).
[57] W. R. Tyson and W. A. Miller, Surf. Sci. **62**, 267 (1977).
[58] J. H. Larsen, J. T. Ranney, D. E. Starr, J. E. Musgrove, and C. T. Campbell, Phys. Rev. B **63**, 195410 (2001).
[59] J. Purton, S. C. Parker, and D. W. Bullet, J. Phys.: Condens. Matter **9**, 5709 (1997).
[60] F. Didier and J. Jupille, J. Adhes. **58**, 253 (1996).
[61] C. Li, R. Wu, A. J. Freeman, and C. L. Fu, Phys. Rev. B **48**, 8317 (1993).
[62] T. Hong, J. R. Smith, and D. J. Srolovitz, Acta Metall. Mater. **43**, 2721 (1995).
[63] M. W. Finnis, J. Phys.: Condens. Matter **8**, 5811 (1996).
[64] Y. F. Zhukovskii, M. Alfredsson, K. Hermansson, E. Heifets, and E. A. Kotomin, Nucl. Instrum. Methods Phys. Res. B **141**, 73 (1998).
[65] U. Schönberger, O. K. Andersen, and M. Methfessel, Acta Metall. Mater. **40**, S1 (1992).